Hierarchical Refinement of Microkinetic Models: Assessment of the Role of the WGS and r-WGS Pathways in CH_4 Partial Oxidation on Rh

Matteo Maestri,* Dario Livio, Alessandra Beretta, and Gianpiero Groppi

Laboratory of Catalysis and Catalytic Processes, Dipartimento di Energia, Politecnico di Milano, Piazza Leonardo da Vinci 32, 20133 Milano, Italy

1. INTRODUCTION

Detailed microkinetic modeling of heterogeneous catalysis is quite rapidly becoming a widely applied tool for the analysis and design of catalytic processes.[1−11] Such models are relevant and useful because, unlike classical kinetic models, they do not require a priori assumptions about the rate-determining step (RDS) and the most abundant surface intermediate (MASI). Consequently, in principle, they can capture the kinetics of a reacting system under significantly different operating conditions and represent a unique tool for both the analysis of reaction mechanisms and advanced process design.[12,13] Key in this respect is the achievement of a quantitative description not only of the experimental data but also of the predicted catalytic cycle, which must be consistent with the macroscopic observed kinetic behavior.[14,15] The predicted catalytic cycle is the result of the interplay among the rates of *all* of the elementary steps, which are responsible for the production and consumption of the reacting intermediates. As a consequence, the performances of a microkinetic model are determined not by the individual elementary steps but by each elementary step *interacting with the others*. Therefore, there is a clear need for consistency among the rate parameters of each elementary step, which poses severe challenges for the development of predictive microkinetic models.

In principle, the estimation of rate parameters is the realm of electronic structure theory calculations, which explicitly treat the quantum-mechanical nature of the chemical bond.[16] On one hand, such studies are of great relevance in revealing specific features of the reaction mechanism (see, e.g., refs 17 and 18). On the other hand, the application of quantum-chemical calculations is still far from optimal in the development of quantitative microkinetic models for complex catalytic processes. In particular, the lack of awareness of the current possibilities of first-principles calculations in this specific context leads to either profound skepticism or unrealistic expectations about the use of such studies in practical systems.[19] This is mainly related to two different issues: First, the insufficient accuracy of the underlying methods used for the solution of a quantum-mechanical problem [e.g., the density-functional theory (DFT) exchange correlation functional used] can lead to unacceptable errors in the reaction rates. As an example, a generic uncertainty for reaction energies of semilocal DFT can be estimated on the order of 0.2−0.3 eV, which implies an uncertainty in rate constants of 1−3 orders of magnitude at temperatures in the range of 400−600 K.[19,20] Second, the intrinsic uncertainty in the structures of the catalysts and active sites along with the appropriate accounting for coverage effects can strongly limit the transferability of the calculated results to “practical” systems under the actual conditions of temperature, pressure, gas composition, and concomitant surface coverage. Moreover, the treatment of all of these aspects with a pure first-principles approach would be beyond any practical expectation and prohibitive for most processes of real technological interest.[21]

Received: April 17, 2014
Revised: June 9, 2014
Accepted: June 10, 2014
Published: June 10, 2014

Hierarchical multiscale approaches, pioneered by Vlachos and co-workers,[16,22,23] represent a very promising methodology to enable the development of microkinetic models that quantitatively incorporate insights from first-principles calculations. The main feature of this methodology consists of tackling the problem with an increasing level of accuracy (and required computational time) by hierarchically combining semiempirical methods with first-principles calculations in the microkinetic analysis of kinetically relevant experiments.[2,16] A schematic representation of the methodology is provided in Figure 1.

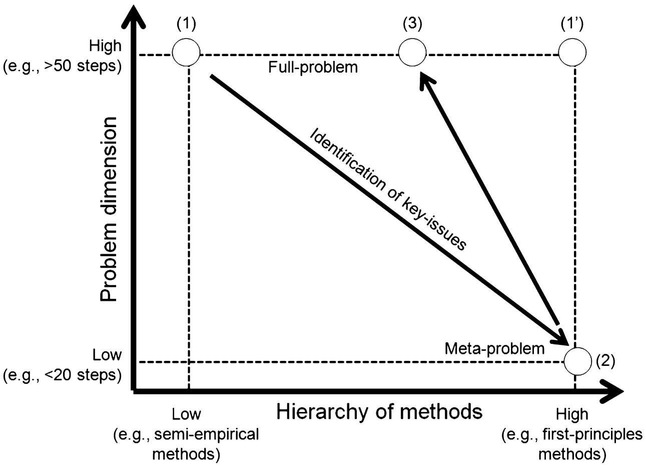

Figure 1. Schematic representation of the hierarchical approach for microkinetic model development.

A semiempirical method (point 1 in Figure 1) is first used to estimate the kinetic parameters for the full problem. In particular, the semiempirical model is used to rapidly estimate barriers under the local conditions of surface coverage in the reactor, which would be otherwise not tractable with higher-accuracy methods (point 1′ in Figure 1).[21,24,25] Next, upon the solution of the microkinetic model in the simulation of kinetically relevant experiments, reaction path analysis (RPA) and identification of the most abundant surface intermediates (MASIs) allow for the derivation of the dominant reaction steps forming the catalytic cycle. Sensitivity analysis (SA) is also used to identify the most sensitive parameters with respect to model predictions. Only these dominant steps are then refined with first-principles methods (point 2 in Figure 1). In this way, such studies are guided to the relevant parts of the reaction network and provide peculiar insights such as the identification of possible errors in the catalytic mechanism or model assumptions. The last step (from point 2 to point 3 in Figure 1) encompasses the incorporation of the insights from first-principles calculations into the semiempirical framework to yield a first-principles refined microkinetic model.

In previous works, we applied the hierarchical multiscale approach for the development of a C_1 microkinetic model for the conversion of CH_4 to syngas on Rh that was able to quantitatively predict the behaviors of different reacting systems, including steam reforming (SR), dry reforming (DR), and partial oxidation (CPO).[1] Nevertheless, microkinetic analysis of spatially resolved adiabatic partial oxidation on foams clearly pointed out the major weakness of the model, which was related to an unsatisfactory mechanistic description of the water−gas-shift (WGS) and reverse water−gas-shift (r-WGS) reacting systems.[26] Following the hierarchical multiscale approach, Maestri and Reuter[14] showed, through first-principles calculations, that this incorrect prediction of the WGS/r-WGS systems was associated with an erroneous assumption in the description of one elementary step and derived catalytic cycles consistent with the experimental evidence.

The main point, however, still unanswered and the subject of the present article, is related to the *quantitative* incorporation of the information derived from first-principles modeling into the overall microkinetic model and its reconciliation with the complexity of the reacting system (point 3 in Figure 1). This is crucial to transfer the insights from first-principles methods to complex processes in "practical" catalysis.

In particular, in this work, we present a hierarchical first-principles refinement of the microkinetic model of Maestri et al.[1] for the description of CH_4 conversion on Rh guided by the DFT-based analysis of the WGS/r-WGS pathways.[14] Modification and refinement of the microkinetic model are carried out on the basis of a comprehensive set of isothermal experimental data. Extensive validation of the microkinetic model with respect to system complexity is thoroughly discussed and assessed through the analysis of spatially resolved experiments of partial oxidation on foams under different conditions of CO_2 and H_2O cofeed.

2. METHODOLOGY

The hierarchical refinement proposed by Vlachos and co-workers[1,2,27] is used to quantitatively introduce into the microkinetic model the information derived from first-principles calculations. For different experimental conditions, we identify the catalytic cycle through RPA based on the net consumption rate of the reacting intermediates. Unlike RPA based on only enthalpy diagrams, the derivation of the dominant mechanism using species net consumption rates incorporates both entropic and enthalpic contributions along with the available chemical activity (mass action) under the specific operating conditions.

The consistency of the dominant mechanism with the experimental information is then assessed in terms not only of quantitative predictions but also of macroscopic kinetic behavior. In particular, this assessment entails the identification of the RDS for the reaction network by the means of equilibrium analysis and sensitivity analysis.[28−30] The parameters of the underlying semiempirical method are then modified on the basis of the insights from higher-accuracy methods to achieve full consistency with the experimental information.

Within this scope, we used a comprehensive set of isothermal experimental tests performed in an annular reactor.[31,32] We simulated the experimental data using a one-dimensional heterogeneous mathematical model accounting for the experimental temperature profile in each simulation.[33] The mean-field microkinetic model was incorporated into the reactor model by using the catalyticSMOKE libraries.[34,35] In each simulation, we considered the specific number of active sites as an independent input calculated from chemisorption experiments. The catalyst weight was on the order of 10 mg (4% Rh/α-Al_2O_3), and the Rh dispersion for the catalyst was estimated to be 5% from CO and H_2 chemisorption experiments.[36]

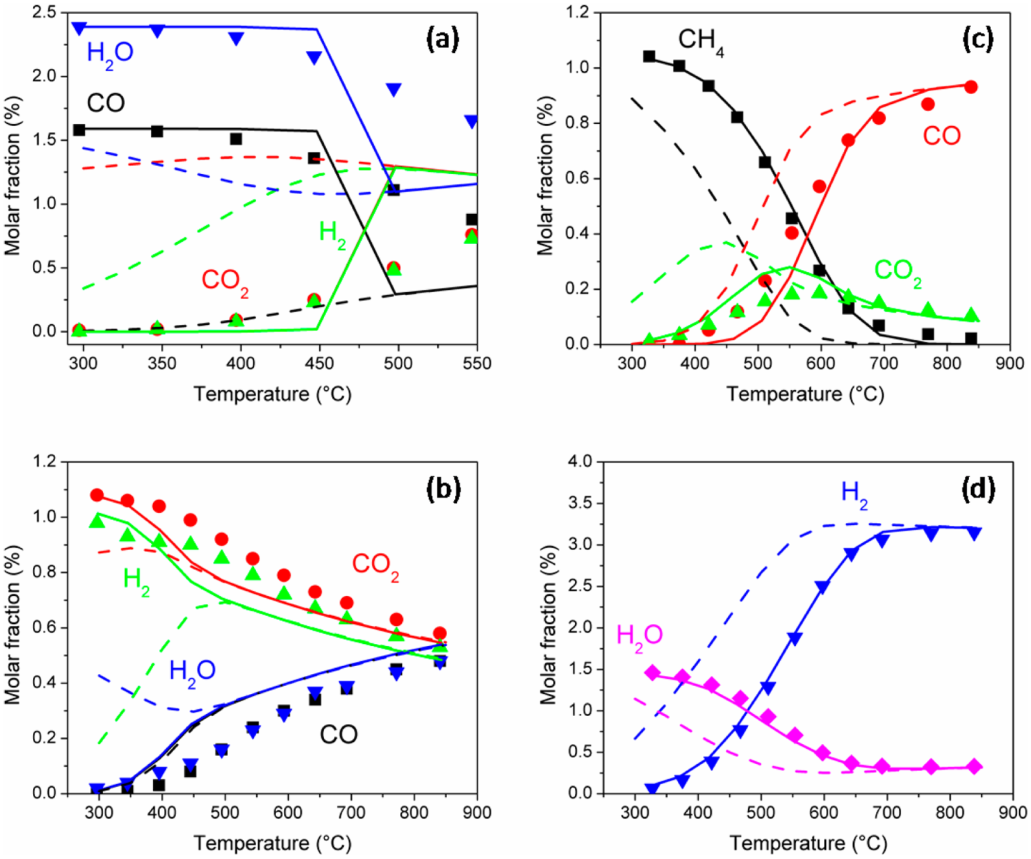

Figure 2. Predictions of the microkinetic model of Maestri et al.[1] in (a) WGS (CO, 1.59%; H_2O, 2.39%), 0.01274 mol/min; (b) r-WGS (CO_2, 1.02%; H_2, 1.09%), 0.01321 mol/min; (c,d) SR (CH_4, 1.04%; H_2O, 1.49%), 0.01670 mol/min, balance N_2. Symbols are experimental data, solid lines are model calculations, and dashed lines are equilibrium values. Annular reactor: i.d., 4 mm; o.d., 5 mm; length, 22 mm.

3. RESULTS AND DISCUSSION

3.1. Quantitative Assessment of Original Model Performance.

We start our analysis by considering SR and WGS/r-WGS experiments.[31] Figure 2 shows comparisons between the semiempirical model of Maestri et al.[1] (hereafter referred to as the original model) and experiments on the WGS (panel a), r-WGS (panel b), and SR (panels c and d). On one hand, the CH_4 consumption and H_2 production are well predicted over the whole range of temperatures in SR (Figure 2c,d). On the other hand, overestimation of CO_2 and underestimation of CO at intermediate temperatures (500–600 °C) is observed (Figure 2c). These results are consistent with the WGS/r-WGS predictions shown in Figure 2a,b. In fact, the original model underestimates the WGS and r-WGS at low temperature (<450 °C), where the catalyst surface is fully covered by CO* and CH* species (the superscript * hereafter refers to adsorbed species). Then, at 450 °C, a sharp increase in activity is predicted, such that the model suddenly reaches the equilibrium composition in contrast to what is experimentally observed. This leads, far from thermodynamic equilibrium, to predicted macroscopic reaction orders in the WGS/r-WGS that are not in agreement with the experimental observations reported by Donazzi et al.[31] In particular, Donazzi et al. found that, to reproduce the experimental trends correctly, they had to invoke two different rate equations for the WGS and r-WGS far from thermodynamic equilibrium, thus implying the occurrence of different dominant elementary steps for the forward and reverse reactions.

Such a feature is not reproduced by the original microkinetic model, where the predicted catalytic cycles for both the WGS and r-WGS encompass the step CO* + OH* ↔ CO_2* + H*. Indeed, the DFT calculations of Maestri and Reuter[14] revealed that the reaction CO* + OH* → CO_2* + H*) is *not elementary* (i.e., it does not occur in one single step), but rather proceeds through the formation of stable carboxyl intermediates.[14] A summary of the insights from the first-principles analysis is provided in Figure 3.

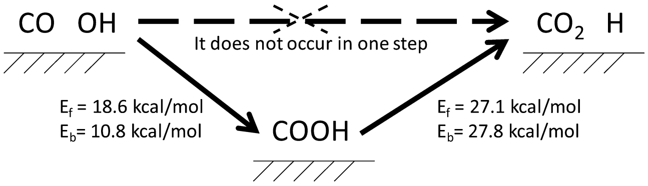

Figure 3. Schematic summary of the first-principles analysis. Level of theory: DFT-PBE, ultrasoft pseudopotential, 2 × 2 three-layer Rh(111) supercell. Details in ref 14.

3.2. Refinement of the Semiempirical Microkinetic Model.

We now aim to quantitatively include the insights from first-principles analysis in the semiempirical microkinetic model. First, the microscale (i.e., the whole ensemble of the elementary steps) is modified by removing the false elementary step (R_{29-30}, CO* + OH* ↔ CO_2* + H*) from the microkinetic model (Figure 3). The set of elementary steps included in the revised microkinetic model is reported in Table

Table 1. First-Principles Hierarchically Refined Microkinetic Model

no.	reaction	A (unitless or s^{-1})	β	bond index, ϕ	activation energy (kcal/mol)
1	$H_2 + 2^* \rightarrow 2H^*$	7.73×10^{-1}	0.9387	0.5	0.0
2	$2H^* \rightarrow H_2 + 2^*$	5.56×10^{11}	−0.4347	0.5	$20.4 - 5\theta_H - 7.4\theta_{CO} + f(T)$
3	$O_2 + 2^* \rightarrow 2O^*$	4.81×10^{-2}	1.9965	0.5	0.0
4	$2O^* \rightarrow O_2 + 2^*$	4.31×10^{12}	1.1995	0.5	$80.9 - 52.0\theta_O + f(T)$
5	$OH^* + {}^* \rightarrow H^* + O^*$	1.82×10^{14}	−0.2659	0.7	$\phi[\Delta H_{r,gas} + Q_{OH} - Q_O - Q_H + Q_O Q_H/(Q_O + Q_H)]$
6	$H^* + O^* \rightarrow OH^* + {}^*$	1.64×10^{14}	−0.8196	0.7	$E_5 - (\Delta H_{r,gas} + Q_{OH} - Q_O - Q_H)$
7	$H_2O^* + {}^* \rightarrow H^* + OH^*$	1.15×10^{11}	0.0281	0.55	$\phi[\Delta H_{r,gas} + Q_{H_2O} - Q_{OH} - Q_H + Q_{OH} Q_H/(Q_{OH} + Q_H)]$
8	$H^* + OH^* \rightarrow H_2O^* + {}^*$	3.60×10^{8}	1.2972	0.55	$E_7 - (\Delta H_{r,gas} + Q_{H_2O} - Q_{OH} - Q_H)$
9	$2OH^* \rightarrow H_2O^* + O^*$	7.22×10^{10}	−0.2902	0.8	$\phi[\Delta H_{r,gas} + 2Q_{OH} - Q_{H_2O} - Q_O + Q_{H_2O} Q_O/(Q_{H_2O} + Q_H)]$
10	$H_2O^* + O^* \rightarrow 2OH^*$	2.08×10^{13}	−2.1130	0.8	$E_9 - (\Delta H_{r,gas} + 2Q_{OH} - Q_{H_2O} - Q_O)$
11	$OH + {}^* \rightarrow OH^*$	2.66×10^{-1}	−0.2891	0.5	0.0
12	$OH^* \rightarrow OH + {}^*$	1.14×10^{13}	−0.9500	0.5	$70.0 - 33.0\theta_O - 25.0\theta_{H_2O} + f(T)$
13	$H_2O + {}^* \rightarrow H_2O^*$	7.72×10^{-2}	1.4067	0.5	0.0
14	$H_2O^* \rightarrow H_2O + {}^*$	2.06×10^{13}	−1.8613	0.5	$10.8 - 25.0\theta_{OH} - 4.5\theta_{H_2O} + f(T)$
15	$H + {}^* \rightarrow H^*$	1.93×10^{-1}	1.5313	0.5	0.0
16	$H^* \rightarrow H + {}^*$	2.40×10^{12}	1.3208	0.5	$62.3 - 2.5\theta_H - 3.7\theta_{CO} + f(T)$
17	$O + {}^* \rightarrow O^*$	4.46×10^{-2}	−1.9236	0.5	0.0
18	$O^* \rightarrow O + {}^*$	9.74×10^{12}	−1.9701	0.5	$100.0 - 26.0\theta_O + f(T)$
19	$CO + {}^* \rightarrow CO^*$	5.00×10^{-1}	−2.0000	0.5	0.0
20	$CO^* \rightarrow CO + {}^*$	5.65×10^{12}	1.9879	0.5	$38.5 - 3.7\theta_H - 15.0\theta_{CO} + f(T)$
21	$CO_2 + {}^* \rightarrow CO_2^*$	3.67×10^{-1}	−2.3294	0.5	0.0
22	$CO_2^* \rightarrow CO_2 + {}^*$	7.54×10^{10}	2.1831	0.5	$5.2 + f(T)$
23	$CO_2^* + {}^* \rightarrow CO^* + O^*$	8.24×10^{9}	1.9698	0.44	$\phi[\Delta H_{r,gas} + Q_{CO_2} - Q_{CO} - Q_O + Q_{CO} Q_O/(Q_{CO} + Q_O)]$
24	$CO^* + O^* \rightarrow CO_2^* + {}^*$	6.54×10^{9}	1.3560	0.44	$E_{23} - (\Delta H_{r,gas} + Q_{CO_2} - Q_{CO} - Q_O)$
25	$COOH + {}^* \rightarrow COOH^*$	5.34×10^{-1}	−1.0767	0.5	0.0
26	$COOH^* \rightarrow COOH + {}^*$	1.12×10^{11}	1.6803	0.5	$62.2 + f(T)$
27	$HCOO + 2^* \rightarrow HCOO^{**}$	1.89×10^{-2}	−0.5548	0.5	0.0
28	$HCOO^{**} \rightarrow HCOO + 2^*$	3.74×10^{13}	0.5548	0.5	$69.2 + f(T)$
~~29~~[a]	~~$CO_2^* + H^* \rightarrow CO^* + OH^*$~~				
~~30~~	~~$CO^* + OH^* \rightarrow CO_2^* + H^*$~~				
31	$COOH^* + {}^* \rightarrow CO^* + OH^*$	1.07×10^{12}	−0.4123	0.5	$\phi[\Delta H_{r,gas} + Q_{COOH} - Q_{CO} - Q_{OH} + Q_{CO} Q_{OH}/(Q_{CO} + Q_{OH})]$
32	$CO^* + OH^* \rightarrow COOH^* + {}^*$	9.37×10^{11}	0.4123	0.5	$E_{31} - (\Delta H_{r,gas} + Q_{COOH} - Q_{CO} - Q_{OH})$
33	$COOH^* + {}^* \rightarrow CO_2^* + H^*$	1.00×10^{10}	−0.4424	0.9	$\phi[\Delta H_{r,gas} + Q_{COOH} - Q_{CO_2} - Q_H + Q_{CO_2} Q_H/(Q_{CO_2} + Q_H)] + 15_b$
34	$CO_2^* + H^* \rightarrow COOH^* + {}^*$	9.99×10^{9}	0.4424	0.9	$E_{34} - (\Delta H_{r,gas} + Q_{COOH} - Q_{CO_2} - Q_H) + 15_b$
35	$CO^* + H_2O^* \rightarrow COOH^* + H^*$	3.34×10^{11}	−0.2222	0.9	$\phi[\Delta H_{r,gas} + Q_{CO} + Q_{H_2O} - Q_{COOH} - Q_H + Q_{COOH} Q_H/(Q_{COOH} + Q_H)]$

Table 1. continued

no.	reaction	A (unitless or s^{-1})	β	bond index, ϕ	activation energy (kcal/mol)
36	$COOH^* + H^* \rightarrow CO^* + H_2O^*$	1.20×10^{9}	0.2223	0.9	$E_{35} - (\Delta H_{r,gas} + Q_{CO} + Q_{H_2O} - Q_{COOH} - Q_{H})$
37	$CO_2^* + OH^* \rightarrow COOH^* + O^*$	1.05×10^{11}	0.7192	0.5	$\phi[\Delta H_{r,gas} + Q_{CO_2} + Q_{OH} - Q_{COOH} - Q_{O} + Q_{COOH}Q_{O}/(Q_{COOH} + Q_{O})]$
38	$COOH^* + O^* \rightarrow CO_2^* + OH^*$	9.51×10^{10}	−0.7192	0.5	$E_{37} - (\Delta H_{r,gas} + Q_{CO_2} + Q_{OH} - Q_{COOH} - Q_{O})$
39	$CO_2^* + H_2O^* \rightarrow COOH^* + OH^*$	1.78×10^{13}	−0.1922	0.01	$\phi[\Delta H_{r,gas} + Q_{CO_2} + Q_{H_2O} - Q_{COOH} - Q_{OH} + Q_{COOH}Q_{OH}$ $/(Q_{COOH} + Q_{OH})]$
40	$COOH^* + OH^* \rightarrow CO_2^* + H_2O^*$	5.60×10^{10}	0.1922	0.01	$E_{39} - (\Delta H_{r,gas} + Q_{CO_2} + Q_{H_2O} - Q_{COOH} - Q_{OH})$
41	$HCOO^{**} \rightarrow CO_2^* + H^*$	3.86×10^{13}	−1.1253	0.5	$\phi[\Delta H_{r,gas} + Q_{HCOO} - Q_{CO_2} - Q_{H} + Q_{CO_2}Q_{H}/(Q_{CO_2} + Q_{H})]$
42	$CO_2^* + H^* \rightarrow HCOO^{**}$	1.04×10^{9}	1.1254	0.5	$E_{41} - (\Delta H_{r,gas} + Q_{HCOO} - Q_{CO_2} - Q_{H})$
43	$CO_2^* + OH^* + * \rightarrow HCOO^{**} + O^*$	1.09×10^{9}	1.4022	0.5	$\phi[\Delta H_{r,gas} + Q_{CO_2} + Q_{OH} - Q_{HCOO} - Q_{O} + Q_{HCOO}Q_{O}/(Q_{HCOO} + Q_{O})]$
44	$HCOO^{**} + O^* \rightarrow CO_2^* + OH^* + *$	3.67×10^{13}	−1.4022	0.5	$E_{43} - (\Delta H_{r,gas} + Q_{CO_2} + Q_{OH} - Q_{HCOO} - Q_{O})$
45	$CO_2^* + H_2O^* + * \rightarrow HCOO^{**} + OH^*$	9.24×10^{9}	0.4908	0.5	$\phi[\Delta H_{r,gas} + Q_{CO_2} + Q_{H_2O} - Q_{HCOO} - Q_{OH} + Q_{HCOO}Q_{OH}$ $/(Q_{HCOO} + Q_{OH})]$
46	$HCOO^{**} + OH^* \rightarrow CO_2^* + H_2O^* + *$	1.08×10^{12}	−0.4908	0.5	$E_{5} - (\Delta H_{r,gas} + Q_{CO_2} + Q_{H_2O} - Q_{HCOO} - Q_{OH})$
47	$C + * \rightarrow C^*$	4.98×10^{-2}	−1.8618	0.5	0.0
48	$C^* \rightarrow C + *$	3.54×10^{4}	1.8618	0.5	$155.0 + f(T)$
49	$CH + * \rightarrow CH^*$	2.29×10^{-2}	−1.0798	0.5	0.0
50	$CH^* \rightarrow CH + *$	3.08×10^{13}	1.0798	0.5	$151.2 + f(T)$
51	$CH_2 + * \rightarrow CH_2^*$	4.09×10^{-2}	−0.4265	0.5	0.0
52	$CH_2^* \rightarrow CH_2 + *$	1.73×10^{13}	0.4265	0.5	$109.3 + f(T)$
53	$CH_3 + * \rightarrow CH_3^*$	1.35×10^{-1}	0.0326	0.5	0.0
54	$CH_3^* \rightarrow CH_3 + *$	5.22×10^{12}	−0.0325	0.5	$42.4 + f(T)$
55	$CH_4 + 2^* \rightarrow CH_3^* + H^*$	5.72×10^{-1}	0.7883	0.5	$\phi[D_g - Q_{CH_4} - Q_{CH_3} - Q_{H} + Q_{CH_3}Q_{H}/(Q_{CH_3} + Q_{H})]$
56	$CH_3^* + H^* \rightarrow CH_4 + 2^*$	7.72×10^{10}	−0.7883	0.5	$E_{59} - (D_g - Q_{CH_4} - Q_{CH_3} - Q_{H})$
57	$CH_3^* + * \rightarrow CH_2^* + H^*$	2.49×10^{10}	0.0862	0.5	$\phi[D_g + Q_{CH_3} - Q_{CH_2} - Q_{H} + Q_{CH_2}Q_{H}/(Q_{CH_2} + Q_{H})]$
58	$CH_2^* + H^* \rightarrow CH_3^* + *$	2.57×10^{9}	−0.0862	0.5	$E_{57} - (D_g + Q_{CH_3} - Q_{CH_2} - Q_{H})$
59	$CH_2^* + * \rightarrow CH^* + H^*$	5.50×10^{10}	−0.1312	0.5	$\phi[D_g + Q_{CH_2} - Q_{CH} - Q_{H} + Q_{CH}Q_{H}/(Q_{CH} + Q_{H})]$
60	$CH^* + H^* \rightarrow CH_2^* + *$	7.27×10^{9}	0.1312	0.5	$E_{59} - (D_g + Q_{CH_2} - Q_{CH} - Q_{H})$
61	$CH^* + * \rightarrow C^* + H^*$	4.58×10^{12}	−0.2464	0.5	$\phi[D_g + Q_{CH} - Q_{C} - Q_{H} + Q_{C}Q_{H}/(Q_{C} + Q_{H})]$
62	$C^* + H^* \rightarrow CH^* + *$	2.18×10^{11}	0.2464	0.5	$E_{61} - (D_g + Q_{CH} - Q_{C} - Q_{H})$
63	$CH_3^* + O^* \rightarrow CH_2^* + OH^*$	2.96×10^{11}	−0.1906	0.5	$\phi[\Delta H_{r,gas} + Q_{CH_3} + Q_{O} - Q_{CH_2} - Q_{OH} + Q_{CH_2}Q_{OH}/(Q_{CH_2} + Q_{OH})]$

Table 1. continued

no.	reaction	A (unitless or s^{-1})	β	bond index, ϕ	activation energy (kcal/mol)
64	$CH_2^* + OH^* \rightarrow CH_3^* + O^*$	3.38×10^{10}	0.1906	0.5	$E_5 - (\Delta H_{r,gas} + Q_{CH_3} + Q_O - Q_{CH_2} - Q_{OH})$
65	$CH^* + OH^* \rightarrow CH_2^* + O^*$	3.83×10^{10}	0.4081	0.5	$\phi[\Delta H_{r,gas} + Q_{CH} + Q_{OH} - Q_{CH_2} - Q_O + Q_{CH_2}Q_O/(Q_{CH_2} + Q_O)]$
66	$CH_2^* + O^* \rightarrow CH^* + OH^*$	2.61×10^{11}	−0.4081	0.5	$E_{65} - (\Delta H_{r,gas} + Q_{CH} + Q_{OH} - Q_{CH_2} - Q_O)$
67	$C^* + OH^* \rightarrow CH^* + O^*$	2.30×10^{10}	0.5232	0.5	$\phi[\Delta H_{r,gas} + Q_C + Q_{OH} - Q_{CH} - Q_O + Q_{CH}Q_O/(Q_{CH} + Q_O)]$
68	$CH^* + O^* \rightarrow C^* + OH^*$	4.35×10^{11}	−0.5232	0.5	$E_{67} - (\Delta H_{r,gas} + Q_C + Q_{OH} - Q_{CH} - Q_O)$
69	$CH_2^* + H_2O^* \rightarrow CH_3^* + OH^*$	5.73×10^{10}	−0.7208	0.5	$\phi[\Delta H_{r,gas} + Q_{CH_2} + Q_{H_2O} - Q_{CH_3} - Q_{OH} + Q_{CH_3}Q_{OH}/(Q_{CH_3} + Q_{OH})]$
70	$CH_3^* + OH^* \rightarrow CH_2^* + H_2O^*$	1.74×10^{9}	0.7208	0.5	$E_{69} - (\Delta H_{r,gas} + Q_{CH_2} + Q_{H_2O} - Q_{CH_3} - Q_{OH})$
71	$CH^* + H_2O^* \rightarrow CH_2^* + OH^*$	6.49×10^{11}	−0.5033	0.5	$\phi[\Delta H_{r,gas} + Q_{CH} + Q_{H_2O} - Q_{CH_2} - Q_{OH} + Q_{CH_2}Q_{OH}/(Q_{CH_2} + Q_{OH})]$
72	$CH_2^* + OH^* \rightarrow CH^* + H_2O^*$	1.54×10^{10}	0.5033	0.5	$E_{71} - (\Delta H_{r,gas} + Q_{CH} + Q_{H_2O} - Q_{CH_2} - Q_{OH})$
73	$C^* + H_2O^* \rightarrow CH^* + OH^*$	9.74×10^{11}	−0.3882	0.5	$\phi[\Delta H_{r,gas} + Q_C + Q_{H_2O} - Q_{CH} - Q_{OH} + Q_{CH}Q_{OH}/(Q_{CH} + Q_{OH})]$
74	$CH^* + OH^* \rightarrow C^* + H_2O^*$	6.41×10^{10}	0.3882	0.5	$E_{73} - (\Delta H_{r,gas} + Q_C + Q_{H_2O} - Q_{CH} - Q_{OH})$
75	$CO^* + * \rightarrow C^* + O^*$	1.25×10^{9}	0.5712	0.5	$\phi[D_g + Q_{CO} - Q_C - Q_O + Q_CQ_O/(Q_C + Q_O)]$
76	$C^* + O^* \rightarrow CO^* + *$	7.22×10^{9}	−0.5712	0.5	$E_{75} - (D_g + Q_{CO} - Q_C - Q_O)$
77	$CO^* + H^* \rightarrow CH^* + O^*$	9.07×10^{9}	0.8176	0.7	$\phi[\Delta H_{r,gas} + Q_{CH_3} + Q_O - Q_{CH_2} - Q_{OH} + Q_{CH_2}Q_{OH}/(Q_{CH_2} + Q_{OH})]$
78	$CH^* + O^* \rightarrow CO^* + H^*$	1.10×10^{12}	−0.8176	0.7	$E_{67} - (\Delta H_{r,gas} + Q_C + Q_{OH} - Q_{CH} - Q_O)$
79	$CO^* + H^* \rightarrow C^* + OH^*$	1.18×10^{12}	0.2944	0.45	$\phi[\Delta H_{r,gas} + Q_{CH_3} + Q_O - Q_{CH_2} - Q_{OH} + Q_{CH_2}Q_{OH}/(Q_{CH_2} + Q_{OH})]$
80	$C^* + OH^* \rightarrow CO^* + H^*$	7.60×10^{12}	−0.2944	0.45	$E_{67} - (\Delta H_{r,gas} + Q_C + Q_{OH} - Q_{CH} - Q_O)$
81	$2CO^* \rightarrow C^* + CO_2^*$	1.11×10^{9}	0.2644	0.9	$\phi[D_g + 2Q_{CO} - Q_C - Q_{CO_2} + Q_CQ_{CO_2}/(Q_C + Q_{CO_2})]$
82	$C^* + CO_2^* \rightarrow 2CO^*$	8.10×10^{9}	−0.2644	0.9	$E_{81} - (D_g + 2Q_{CO} - Q_C - Q_{CO_2})$

[a] This step was removed according to DFT analysis. [b] See eq 1 in the text.

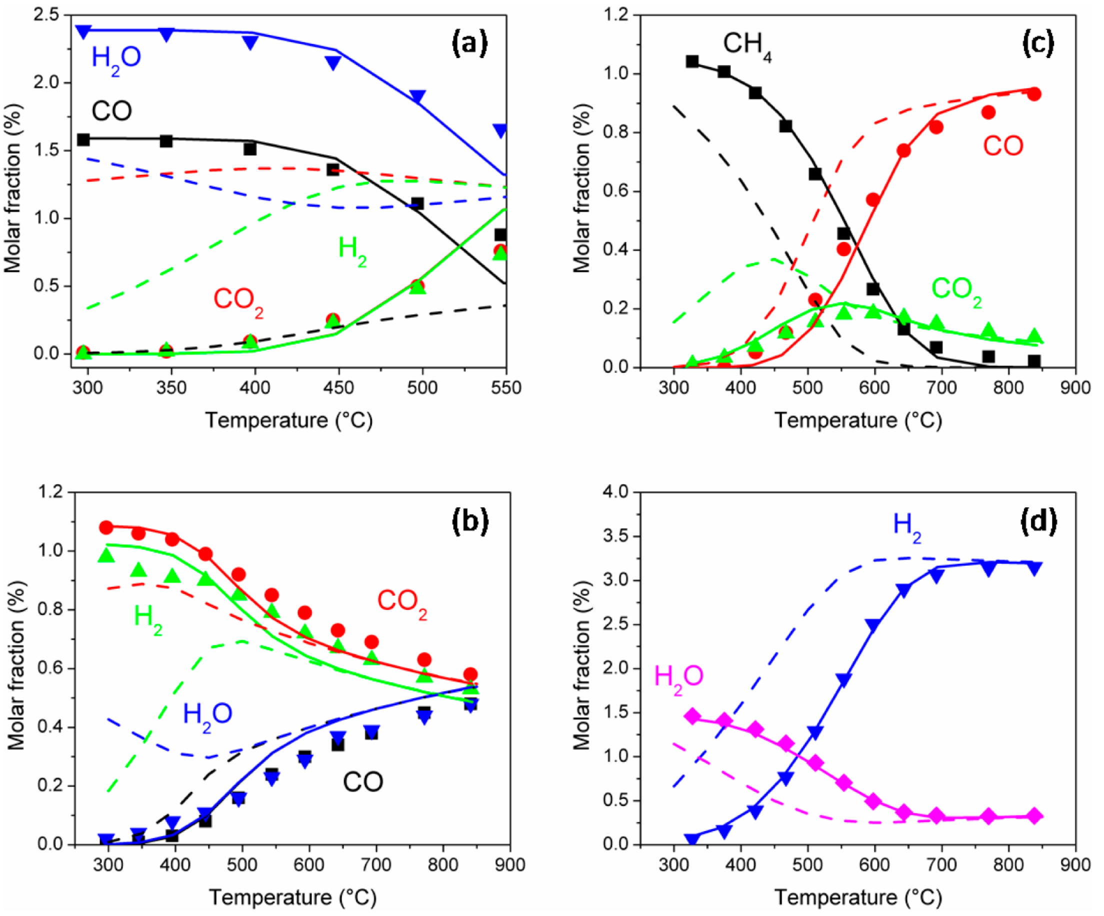

Figure 4. Predictions of the hierarchically refined microkinetic model in (a) WGS (CO, 1.59%; H_2O, 2.39%), 0.01274 mol/min; (b) r-WGS (CO_2, 1.02%; H_2, 1.09%), 0.01321 mol/min; (c,d) SR (CH_4, 1.04%; H_2O, 1.49%), 0.01670 mol/min, balance N_2. Symbols are experimental data, solid lines are model calculations, and dashed lines are equilibrium values. Annular reactor: i.d., 4 mm; o.d., 5 mm; length, 22 mm.

1. All of the activation energies are coverage-dependent within the unity bond index-quadratic exponential potential (UBI-QEP) theory by means of coverage-dependent binding energies. No further addition of elementary steps is required, because the COOH pathway is already taken into account in the original model (R_{31-32} and R_{33-34}). Direct incorporation of the energy barriers calculated with DFT (Figure 3) for this pathway (R_{31-32} and R_{33-34}) is not possible because it would lead to completely unreliable results. In fact, the modification of only some steps would break the internal consistency among the rates of the original microkinetic model, thus leading to completely wrong quantitative and qualitative predictions. The parameters of each elementary step are not optimized per se, but only with respect to the whole set of elementary steps forming the microkinetic model. Therefore, the refinement has to result in an educated modification of the parameters of the semiempirical model driven by insights from first-principles calculations.[21,25,37,38] For instance, within the underlying UBI-QEP semiempirical method, information from the higher-hierarchy methods can be input into the model through the bond index (which retains information on the nature of transition state and has been shown to be crucial for the application of the method at a controlled level of uncertainty[37]) and the heats of chemisorption of the reacting intermediates.

Regarding the activation energy in Table 1, note that the reaction rate constant (k) is calculated as

$$k = \frac{A}{{\Gamma_{\mathrm{Rh}}}^{n-1}}\left(\frac{T}{T_0}\right)^{\beta} \mathrm{e}^{-E/RT} \quad \text{or}$$

$$k = \frac{s}{{\Gamma_{\mathrm{Rh}}}^{n}}\sqrt{\frac{RT}{2\pi \mathrm{MW}}}\left(\frac{T}{T_0}\right)^{\beta} \mathrm{e}^{-E/RT}$$

where A is the pre-exponential, s is the sticking coefficient, Γ_{Rh} is the site density, n is the reaction order, MW is the molecular weight, E is the activation energy, R is the ideal gas constant, and T_0 is the reference temperature (300 K). Activation energies are calculated according to the UBI-QEP framework.[48] In the simulations, Γ_{Rh} was set equal to 2.49×10^{-9} mol/cm^2. $\Delta H_{\mathrm{r,\,gas}}$ is the enthalpy of reaction in the gas phase. Q_i is the heat of chemisorption of the ith species. The corresponding value is reported in Table 1 in the adsorption/desorption steps. The ith reaction rate is calculated according to

$$r_i = k_i \prod_{j=1}^{K_{\mathrm{tot}}} X_j^{\nu_{i,j}} = k_i {\Gamma_{\mathrm{Rh}}}^{n} \prod_{j=1}^{K_{\mathrm{surf}}} \theta_j^{\nu_{i,j}} \quad \text{for surface reaction}$$

or

$$r_i = k_i \prod_{j=1}^{K_{\mathrm{tot}}} X_j^{\nu_{i,j}} = k_i {\Gamma_{\mathrm{Rh}}}^{n} {X_{\mathrm{gas\,species}}}^{\nu_i} \prod_{j=1}^{K_{\mathrm{surf}}} \theta_j^{\nu_{i,j}}$$

for adsorption reaction

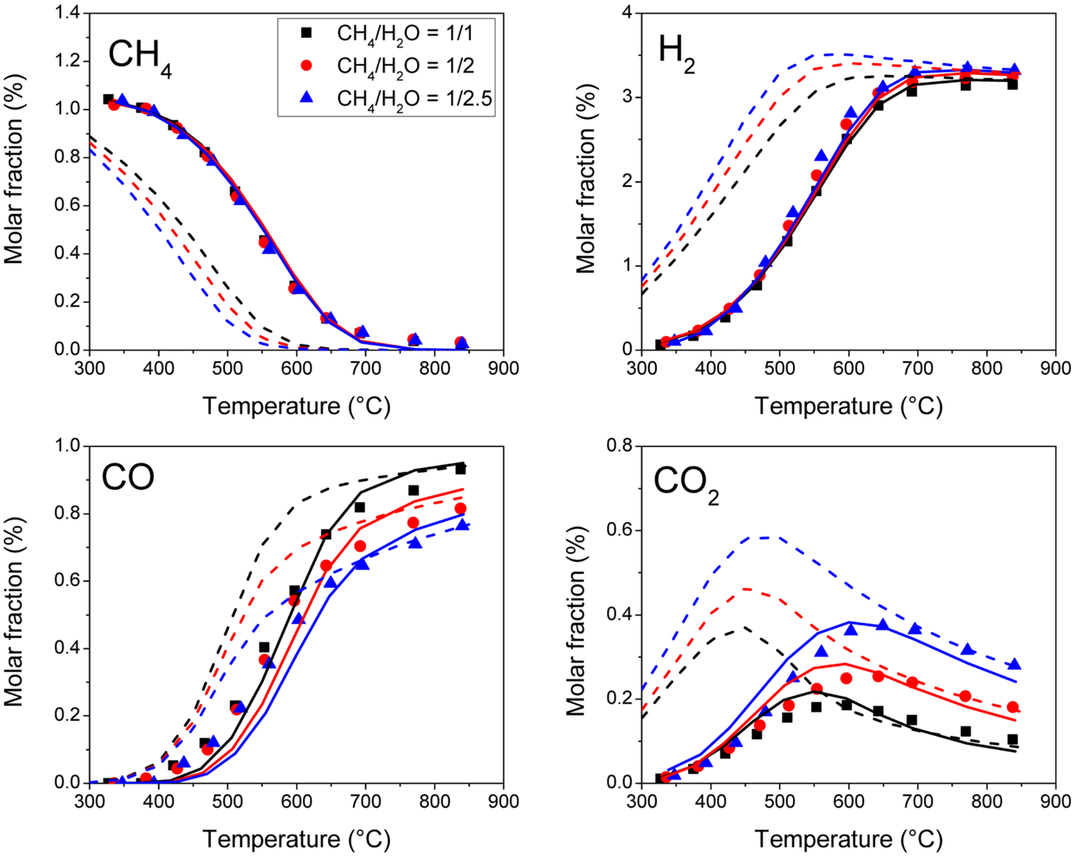

Figure 5. Effect of H_2O inlet molar fraction in SR experiments in an annular reactor. Annular reactor: i.d., 4 mm; o.d., 5 mm; length, 22 mm; balance N_2. Flow rate = 0.01670 mol/min. Symbols are experimental data, solid lines are calculations by the hierarchically refined microkinetic model, and dashed lines are equilibrium values.

where X_j is the mole concentration of either gas species (mol/cm^3) or adspecies (mol/cm^2), θ_j is the site fraction, and r_i is the rate of the ith reaction [mol/(cm^2 s)]. The temperature dependence of the heat of chemisorption was taken into account by statistical mechanics. For details, see ref 1.

First, on the basis of SA and RPA, we identified the relevant elementary steps for the experimental conditions of Figure 2 and refined their bond index on the basis of previous DFT calculations.[14] At low temperature (<400 °C), where CO* adspecies cover up to the 70% of the surface, CO disproportion (R_{81}) is the most sensitive step. Also, the predicted reactivity is too low with respect to experiments, so the bond index for R_{81} is increased from 0.5 to 0.9, in line with the late nature of the transition state of this elementary step.

At higher temperatures, the most relevant steps turn out to be

$$R_{7-8}: \quad H_2O^* + {}^* \leftrightarrow OH^* + H^*$$

$$R_{33-34}: \quad COOH^* + {}^* \leftrightarrow CO_2{}^* + H^*$$

$$R_{39-40}: \quad COOH^* + OH^* \leftrightarrow CO_2{}^* + H_2O^*$$

In particular, the activation energy of elementary step R_{39-40} ($COOH^* + OH^* \leftrightarrow CO_2{}^* + H_2O^*$) is modified by decreasing the bond index to 0.01, on the basis on DFT calculations, which support the evidence of an almost unactivated step.[10] For reactions R_{33-34} ($COOH^* + {}^* \rightarrow CO_2{}^* + H^*$ and its reverse), to reproduce the energetics from DFT at the same level of coverage of the 2 × 2 supercell of Rh(111), an increment of the bond index from 0.5 (default value for a transition state in the standard UBI-QEP method) to 2.2 would be required. If, on one hand, a value higher than 0.5 would agree with the late nature of the transition state revealed by the DFT calculations, on the other hand, a value higher than 1 would not have a direct chemical meaning. In particular, such a value is necessary to compensate the failure of the UBI-QEP potential in describing the minimum-energy path for the dissociation of COOH, which involves a very weakly bounded molecule (CO_2). To overcome this limitation and retain a chemical meaning for the bond index, for this reaction, we followed the approach proposed by Neurock and co-workers,[21] using a constant factor of δ to scale the transition-state energy to match the DFT calculation at the same level of coverage

$$E_{f,d} = E_{f,d}^{UBI} + \delta \qquad (1)$$

Both the forward and reverse reactions are scaled by the same factor δ, thus maintaining unaltered the thermodynamic consistency. In practice, the scaling factor represents a correction of the magnitude of the UBI-QEP potential.

After these modifications, RPA shows that the WGS proceeds through a carboxyl mechanism: CO, once adsorbed on the catalyst, reacts with OH*, generated by water adsorption and dissociation (R_7, $H_2O^* + {}^* \rightarrow OH^* + H^*$), to form COOH*. Such a species further reacts with OH* to $CO_2{}^*$ through R_{40}. Also, all of the relevant steps apart from R_7 turn out to be quasi-equilibrated. Therefore, the overall reaction rate of the WGS depends only on the water concentration, which is consistent with the observed reaction orders derived in ref 31 for the same conditions of temperature and composition. Once

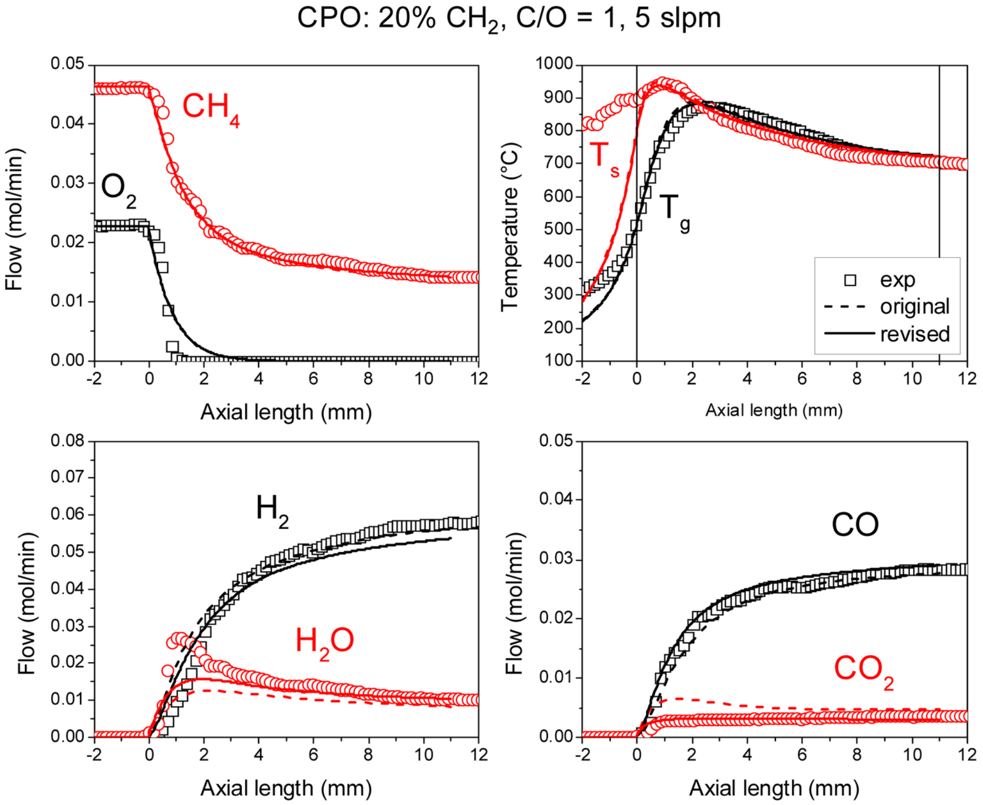

Figure 6. CH_4 CPO over Rh-coated foam. Operating conditions: 20% CH_4, C/O = 1, 5 slpm. Symbols are experimental data, solid lines are calculations by the hierarchically refined microkinetic model, and dashed lines are calculations by the original model.

we have recovered the consistency of the catalytic cycle with respect to the experiments, fine-tuning of the pre-exponential factors within the uncertainty range[13] and bond index is performed to achieve reasonable quantitative agreement with the experimental data. In particular, the bond indexes for reactions R_{5-6} and R_{9-10} are set to 0.7 and 0.8, respectively, in line with the late nature of the corresponding transition states.[37]

Figure 4a shows the performance of the hierarchically refined microkinetic model in terms of quantitative prediction of the experiments. It is evident that the revised description of WGS chemistry leads to a marked improvement in the description of the experimental data.

It is very important to note that the improvement of the prediction from original to revised model has been achieved without any modification of the rate parameters of the RDS ($H_2O^* + * \rightarrow OH^* + H^*$). This false contradiction clearly points out the critical issue for the development of a microkinetic model. In particular, the previously described modifications of the steps other than the RDS resulted in different distributions of the MASI with a concomitant effect on the rate of the RDS due to mass action kinetics (i.e., availability of free sites *).

The refined set of kinetic parameters for the WGS is now used to test the reliability of the new model in predicting r-WGS experiments. Refinement of the step R_{23-24} ($CO_2^* + * \rightarrow CO^* + O^*$ and its reverse) by decreasing the bond index from 0.9[1] to 0.44 was necessary to make this step the dominant one for the CO_2 consumption. Upon this change, RPA shows that, far from equilibrium (e.g., 500 °C), CO_2 converts to CO through the decomposition route (R_{23}), which also represents the RDS, thus reconciling the model predictions with the experimental findings. Sensitivity analysis also evidences a small residual dependence of the global reaction rate on elementary step R_8, which could become determining under different operating conditions. On the whole, upon the modification derived from first-principles refinement, the microkinetic analysis predicts two different catalytic cycles for the WGS and r-WGS far from thermodynamic equilibrium ($T < 500$ °C), in agreement with the experimental evidence. Near equilibrium (e.g., 650 °C), instead, microscopic reversibility applies, and both the WGS and r-WGS reach the equilibrium composition.

Figure 4b shows the performance of the hierarchically refined microkinetic model with respect to r-WGS experiments. It is evident that the revised description of WGS/r-WGS chemistry leads to a marked improvement in the description of the experimental data. Moreover, the modification of WGS and r-WGS chemistry does not affect the capability of the microkinetic scheme to describe SR experiments. In fact, as shown in Figure 4c,d, the agreement of the simulations with experimental data is very satisfactory over the whole range of temperatures. In particular, we observe an improvement in the description of the CO/CO_2 distribution at intermediate temperatures (500−600 °C) as a result of the improved description of the WGS/r-WGS systems.

Additional tests in an annular reactor by Donazzi et al.[31,32] were used for the assessment and validation of the refined microkinetic scheme. No additional changes of the rate parameters were made by means of the following experimental data.

Figure 5 shows comparisons between the model predictions and the experimental SR data at increasing water inlet concentrations. The agreement is very satisfactory for both reactants and products at different catalyst temperatures. It is

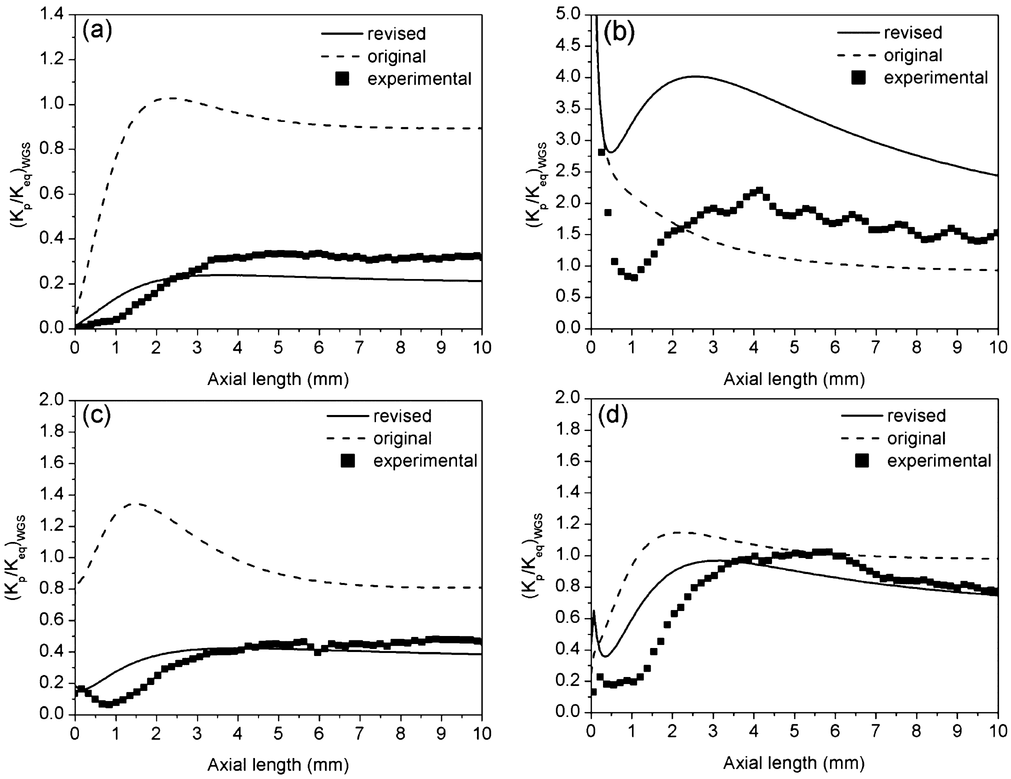

Figure 7. $K_p/K_{equilibrium}$ ratio for the WGS reaction under different operating conditions. C/O = 1; 5slpm; and (a) 20% CH_4, (b) 20% CH_4 + 20% CO_2, (c) 20% CH_4 + 10% H_2O, (d) 20% CH_4 + 10% H_2O + 20% CO_2. Ideal gas mixture of ideal gases. Reference: ideal gas at 1 atm.

worth noting that the revision of the description of the WGS/r-WGS pathways does not modify the macroscopic reaction orders observed in SR. In fact, as Figure 5 illustrates, the refined microkinetic scheme correctly predicts the independence of CH_4 conversion on H_2O molar fraction in the feed mixture.

On the whole, the hierarchical refinement allows information from first-principles analysis to be selectively incorporated into the complex framework of the microkinetic model.

3.3. Analysis of CPO Spatially Resolved Adiabatic Experiments on Foams.

Granted that the hierarchically refined microkinetic model is able to reproduce a broad range of reacting systems under isothermal conditions, we now consider the microkinetic analysis of spatially resolved CPO adiabatic experiments on Rh-coated foams for further validation. In particular, we focused our analysis on the effect of the addition of H_2O and CO_2 to the partial oxidation system to extensively test the reliability of the refined microkinetic model with respect to the WGS and r-WGS routes. Within this scope, we considered the autothermal CH_4 CPO experiments of Schmidt and co-workers[39] over 5 wt % Rh supported on 80 ppi α-Al_2O_3 foams (11-mm length, 17-mm diameter). In the experiments considered herein,[39] the atom balances of C and H closed to ±5% throughout the catalyst, with no observed carbon formation or deactivation for up to 60 h of operation. Also, profiles were replicated on three monoliths. The experiments were analyzed by means of a one-dimensional, heterogeneous, dynamic, fixed-bed reactor model[26] consisting of mass, energy, and momentum balances for the gas and solid phases and including axial convection and solid conduction and gas–solid transport terms. Heat conduction in the solid was described with an effective axial thermal conductivity coefficient for isotropic open-cellular foams[40] corrected by the addition of radiation.[41] The thermal conductivity of the α-Al_2O_3 support was taken as 2 W/(m K).[42] The experimental runs were not perfectly adiabatic.[43] Therefore, a dissipation term was included in the energy balance of the gas phase to account for the heat losses by introducing a global heat-transfer coefficient to match the calculated thermal efficiency (defined as the ratio between the experimental temperature rise and the theoretical adiabatic temperature rise[43]) to the experimental value.[26] The detailed microkinetic model was taken into account in the reactor model by using the catalyticSMOKE libraries.[34,35] For the isothermal runs in the annular reactor, we considered the specific number of active sites as an independent input calculated from chemisorption experiments.[26]

3.3.1. Catalytic Partial Oxidation.

Figure 6 compares the experimental data and model simulations according to both the original and hierarchically refined microkinetic models. On one hand, according to the fact that the refinement of the model affected only elementary steps involving $CO/CO_2/H_2/H_2O$, there are no differences between the predictions of the two microkinetic models in the consumption rates of O_2 and CH_4. On the other hand, clear and crucial differences are apparent in terms of product evolution. In fact, the original microkinetic model (dashed line) overestimates H_2 and CO_2 in the oxidation zone and underestimates CO and H_2. This is in line with the faster approach to WGS equilibrium of the model, which was not observed in the experimental data. Noticeably, the values of the $K_p/K_{equilibrium}$ ratio for the WGS are considerably lower than 1 in the case of the experiments, as reported in Figure 7a. In contrast, based on the original model prediction, $K_p/K_{equilibrium}$ for the WGS rapidly reaches values close to 1. This gives rise to a peak in CO_2 production that is not present in the experimental data.

A consistent improvement in the capability of the model is evident upon the modification derived from first-principles

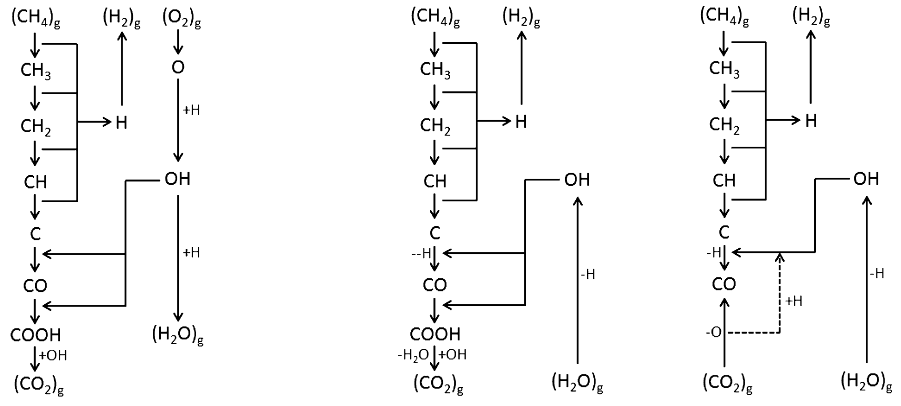

(a)
Oxidation zone (0.5 mm)

(b)
(c)
Reforming zone (4 mm)

Figure 8. Reaction path analysis for (a) oxidation and (b,c) reforming zones. Predicted dominant pathways in the reforming zone are reported for (b) CPO, CPO/H_2O, and CPO/H_2O/CO_2 and (c) CPO/CO_2.

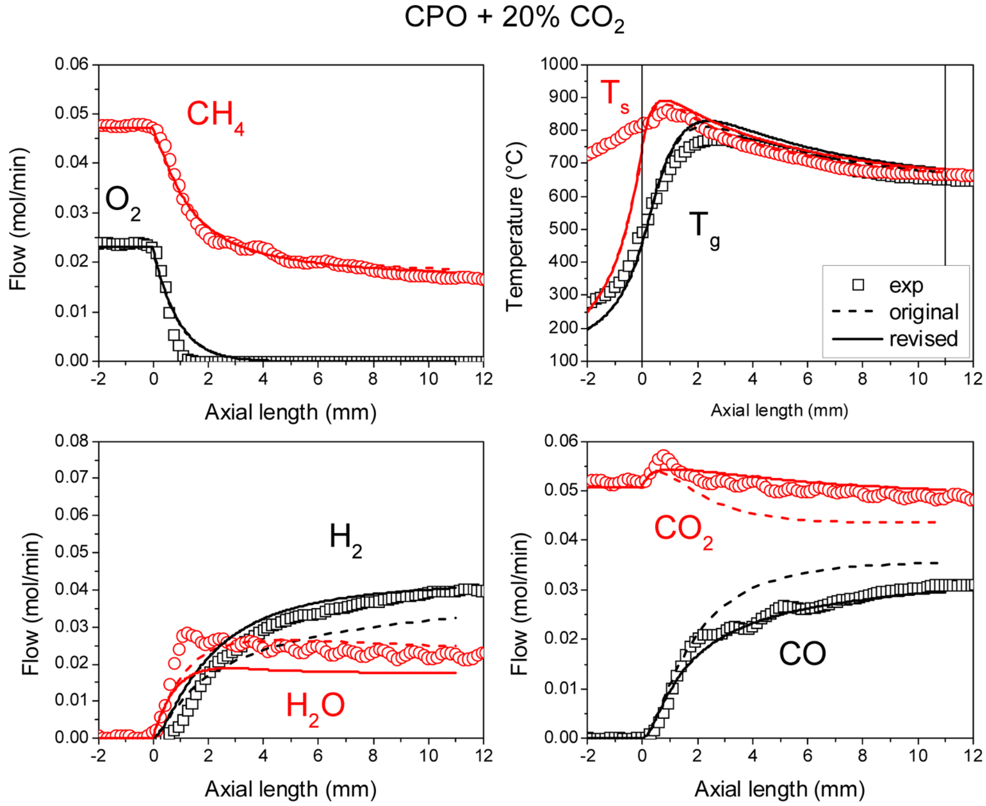

Figure 9. CH_4 CPO over Rh-coated foam with 20% CO_2 cofeeding. Operating conditions: 20% CH_4, C/O = 1 + 20% CO_2, 5 slpm. Symbols are experimental data, solid lines are calculations by the hierarchically refined microkinetic model, and dashed lines are calculations by the original model.

modeling. In particular, the $K_p/K_{\text{equilibrium}}$ ratio for the WGS based on the refined microkinetic model is in full agreement with the experimental trend (Figure 7a). As a consequence, the prediction of the refined microkinetic model (solid line) agrees with experimental trend for product evolution, and the peak in CO_2 disappears. Still, the peak in H_2O, which is also present in the experiments, is not quantitatively reproduced by the model. Because the CO/CO_2 ratio is now well reproduced, the disagreement in the H_2O peak between 1 and 1.5 mm is mainly related to the overestimation of the length of the oxidation zone predicted by the model. Unlike the simulations, the experimental data show a sharper drop in O_2 molar flow. In particular, because oxygen consumption on Rh (differently unlike that on Pt[44]) has been confirmed to be fully mass-transfer-limited,[45] the disagreement in the oxidation zone can be related to variations in the local transport properties due to local variations in the foam structure.[26]

In terms of surface coverage (not shown), more than 80% of the Rh sites are empty, and the remaining 20% are occupied by H* (15%) and CO* (5%). RPA reveals that, even with the revised model, the main routes of product formation are in line with regime II and regime III, reported by Maestri et al.,[45] as shown in Figure 8 for the oxidation and reforming zones. In the part of the reactor where oxygen is still present in the gas phase

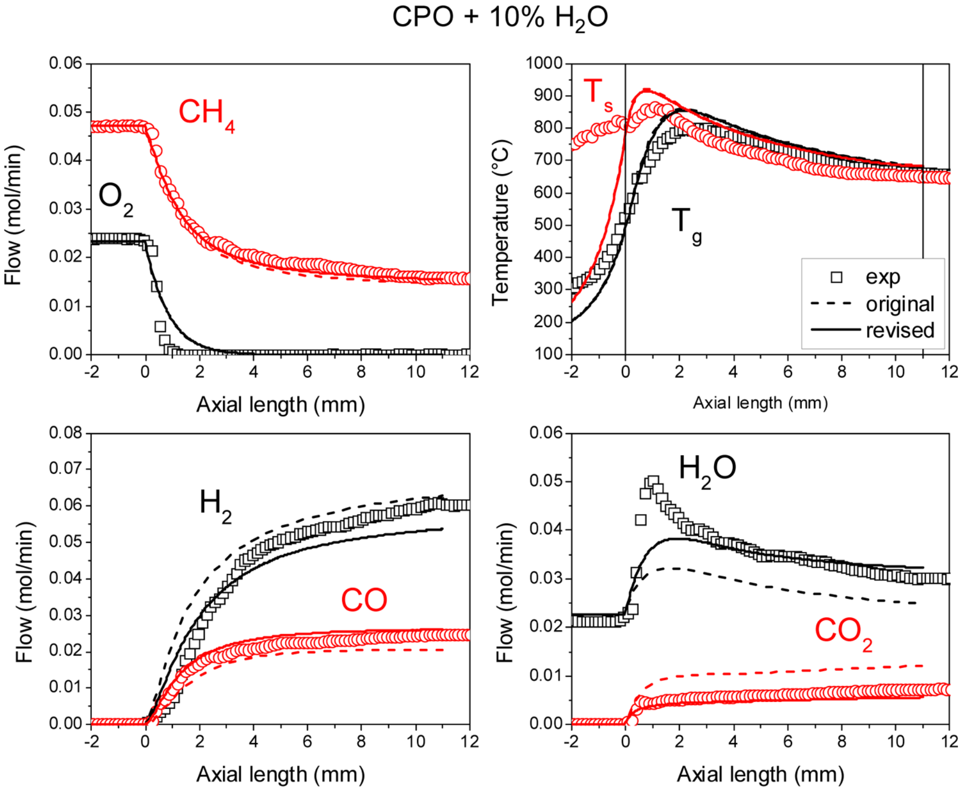

Figure 10. CH_4 CPO over Rh-coated foam with 10% H_2O cofeeding. Operating conditions: 20% CH_4, C/O = 1 + 10% H_2O, 5 slpm. Symbols are experimental data, solid lines are calculations by the hierarchically refined microkinetic model, and dashed lines are calculations by the original model.

(oxidation zone, Figure 8a), CH_4 is consumed by a surface dissociation route to carbon adatoms. CH dissociation turns out to be highly favored (i.e., proceeds at a higher rate) than CH oxidation due to mass action. In fact, oxidation reactions (e.g., R_{67-68}) are not favored because of the very low coverage of oxygen at the surface. Carbon adatoms are then oxidized to CO* and CO_2* through OH*. As a consequence, CO and H_2 are formed by SR, whereas CO_2 is formed by the WGS. The fact that methane consumption is not affected by the wrong prediction of the length of the oxidation zone is in line with the fact that, in the oxidation zone, the oxygen consumption affects only the H_2 and H_2O stoichiometry (Figure 8a). The observed coexistence of $CO/H_2/O_2$ in the bulk of the gas phase is strictly due to the fact that O_2 consumption is fully mass-transfer-controlled. At the catalyst surface, the O_2 concentration drops to zero, and syngas production is observed, in line with the findings of ref 17. The improved microkinetic description of the WGS pathways in the revised model, unlike the original model, allows a quantitative agreement with the experimental rate of formation of CO_2 to be achieved.

Once O_2 is completely consumed (regime III), the dominant reaction path is almost identical to that of the oxidation zone. The only difference holds in the source of the main oxidizer OH* at the surface, which becomes H_2O*, as shown in Figure 8b.

3.3.2. Effect of CO_2 and H_2O Cofeed on Partial Oxidation.

We now consider the effect of CO_2 or H_2O cofeed on partial oxidation. Comparisons between model and experiments are reported in Figure 9 for the case of a cofeed of 20% CO_2 and in Figure 10 for the case of a cofeed of 10% H_2O.

Unlike the original microkinetic model (dashed line), the refined microkinetic model (solid line) is able to predictively reproduce the spatial evolution for both products and reactants. As in the experiments, the microkinetic model does not predict kinetic effects of CO_2 or H_2O on the rate of CH_4 consumption. For a cofeed of both CO_2 and of H_2O, the main dominant pathways in the oxidation zone of the reactor are not affected by the coreactant. In particular (Figure 8a), methane is consumed by a dissociation route, which is the limiting step, and the main oxidizer OH is formed from the reaction between H* and O*, which is fully mass-transfer-limited. This is in line with independent kinetic studies that experimentally confirmed the independence of CH_4 reforming rates from the coreactant.[46,47]

Even under these conditions, dramatic differences are clear between the original and refined models in terms of the product distribution along the axial coordinate. In particular, as is apparent from Figure 7b,c, the WGS turns out to be fully equilibrated for the original model. The refined microkinetic model, instead, predicts WGS compositions in agreement with the experimental evidence. Moreover, in contrast to the oxidation zone, the coreactant markedly influences the product distribution. On one hand, for the case of CO_2 as a coreactant, CO_2* is consumed through its dissociation to CO* and O* in the reforming zone. Then, O* further reacts with H* to give OH* and eventually H_2O* (Figure 8c). Therefore, CO and H_2O increase at the expense of H_2, according to the r-WGS route. Consequently, in the first part of the reactor, the WGS prevails, and CO_2 is produced. In the second part of the reactor, instead, the r-WGS prevails, and CO_2 is consumed. This explains the peak in CO_2 profile. The refined model is able to quantitatively follow the CO_2 evolution, which is first produced and then consumed with a zero net production. This behavior was completely missed by the original model, which rapidly

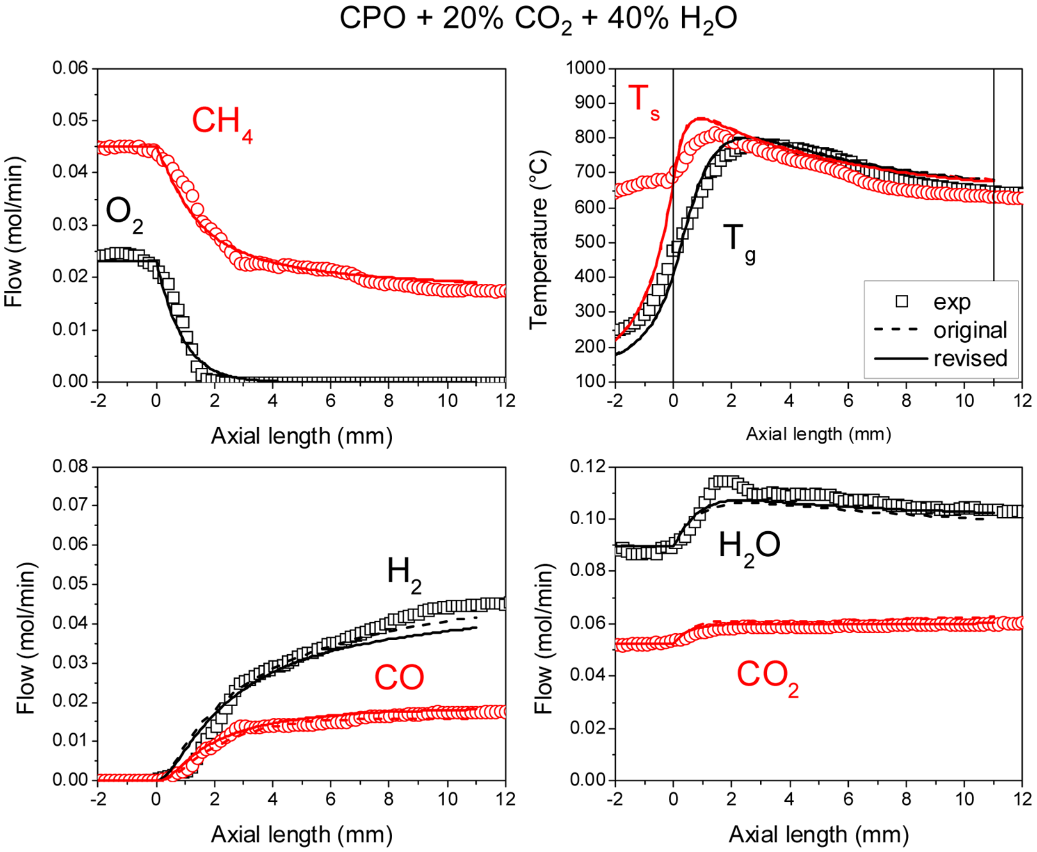

Figure 11. CH_4 CPO over Rh-coated foam with 20% CO_2 and 40% H_2O cofeeding. Operating conditions: 20% CH_4, C/O = 1 + 20% CO_2 and 40% H_2O, 5 slpm. Symbols are experimental data, solid lines are calculations by the hierarchically refined microkinetic model, and dashed lines are calculations by the original model.

reached thermodynamic equilibrium of the WGS (Figure 7b). Therefore, the microkinetic analysis of these experiments clearly points out that CO_2 is consumed by r-WGS routes and does not directly influence the rate of CH_4 consumption. This provides further evidence that the CH_4/CO_2 reacting system on Rh is a combination of SR and r-WGS.[15,32]

On the other hand, H_2O, when is fed as a coreactant, dissociates to OH* and H*. The excess of OH*, which is not consumed by the reaction with C* adatoms generated by the CH_4 dissociation route, further reacts with CO* to CO_2*, through the formation of COOH* intermediates. As a result, H_2 increases at the expense of CO following a WGS route (Figure 8b).

Figure 11 reports the case of simultaneous cofeeding of H_2O and CO_2. Unlike in the CO_2-rich tests, the simultaneous feeding of CO_2 and H_2O does not result in any peak in the CO_2 profile. In fact, as is evident from the RPA, H_2O consumption by the WGS prevails over the r-WGS route in the reforming zone, and the CO*-to-CO_2* path becomes dominant over CO_2* dissociation. The dominant pathways are completely analogous to those that occur in partial oxidation (Figure 8b). The only difference is that, under these specific amounts of H_2O and CO_2 cofeed, the WGS turns out to be equilibrated in the reactor, as reported in Figure 7d. Consequently, differences in the predictions of the two microkinetic models in the product distribution are not observed.

Hence, the analysis of the spatially resolved experiments has further assessed the crucial role of the improved microkinetic description for the WGS and r-WGS derived from the first-principles refinement of the original semiempirical model. This modification turned out to be pivotal in explaining quantitatively and qualitatively, in terms of consistency of the dominant reaction pathways, the experimental evidence.

4. CONCLUSIONS

Following a hierarchical approach, we have incorporated information from first-principles calculations into the framework of a semiempirical microkinetic model. This model is able to explain the behavior of the reacting system under significant different conditions, by also predicting the catalytic cycle in full agreement with experimental evidence on the macroscopic reaction orders. We have shown that a proper description of the microscale in terms of elementary steps is crucial for the description of the reacting system under different operating conditions. Particular care and attention have to be given to the selection of the elementary steps when using semiempirical models, which cannot discriminate whether one step is truly elementary or not. Also, the consistency between the kinetic parameters of *all* of the elementary steps included in the microkinetic model is of utmost importance in achieving a reliable model. Therefore, the information obtained with different levels of theory needs to be properly input into the underlying framework, which allows for thermodynamic and kinetic consistencies under different conditions of reaction environment at the surface (pressure, temperature, concentration, coverage effects).

The hierarchical refinement of the microkinetic model turned out to be crucial for the quantitative description of the WGS and r-WGS pathways in the CPO of CH_4 on Rh. In particular, microkinetic analysis of spatially resolved CPO experiments with cofeeds of H_2O and/or CO_2 allowed us to clarify the main pathways involved in the reforming zone in partial oxidation and to assess their kinetic relevance. H_2O is the preferred coreactant for the dissociation of CH_4, and CO_2 does not directly influence the rate of CH_4 consumption. CO_2 consumption and formation are due to only the WGS and r-WGS, which turned out not to be equilibrated in the reforming zones.

On a more general basis, the proposed approach constitutes a promising effective avenue for transferring ab initio predictive quality to a level of system complexity relevant to technological applications. This can provide a unique input for the atomic-scale understanding of complex processes, with a profound impact on the interpretation of the experimental evidence in "practical" catalytic systems.

■ AUTHOR INFORMATION

Corresponding Author

*E-mail: matteo.maestri@polimi.it. Tel.: +39 0223998650.

Notes

The authors declare no competing financial interest.

■ REFERENCES

(1) Maestri, M.; Vlachos, D. G.; Beretta, A.; Groppi, G.; Tronconi, E. A C_1 microkinetic model for the conversion of methane to syngas on Rh/Al_2O_3. *AIChE J.* **2009**, *55*, 993.

(2) Mhadeshwar, A. B.; Vlachos, D. G. Hierarchical Multiscale Mechanism Development for Methane Partial Oxidation and Reforming and for Thermal Decomposition of Oxygenates on Rh. *J. Phys. Chem. B* **2005**, *109*, 16819.

(3) Schwiedernoch, R.; Tischer, S.; Correa, C.; Deutschmann, O. Experimental and numerical study on the transient behavior of partial oxidation of methane in a catalytic monolith. *Chem. Eng. Sci.* **2003**, *58*, 633.

(4) Bera, T.; Thybaut, J. W.; Marin, G. B. Extension of the Single-Event Microkinetic Model to Alkyl Substituted Monoaromatics Hydrogenation on a Pt Catalyst. *ACS Catal.* **2012**, *2*, 1305.

(5) Kumar, P.; Thybaut, J. W.; Teketel, S.; Svelle, S.; Beato, P.; Olsbye, U.; Marin, G. B. Single-Event MicroKinetics (SEMK) for Methanol to Hydrocarbons (MTH) on H-ZSM-23. *Catal. Today* **2013**, *215*, 224.

(6) Hartmann, M.; Maier, L.; Minh, H. D.; Deutschmann, O. Catalytic partial oxidation of iso-octane over rhodium catalysts: An experimental, modeling, and simulation study. *Combust. Flame* **2010**, *157*, 1771.

(7) Karakaya, C.; Deutschmann, O. Kinetics of hydrogen oxidation on Rh/Al_2O_3 catalysts studied in a stagnation-flow reactor. *Chem. Eng. Sci.* **2013**, *89*, 171.

(8) Maier, L.; Schadel, B.; Delgado, K. H.; Tischer, S.; Deutschmann, O. Steam Reforming of Methane Over Nickel: Development of a Multi-Step Surface Reaction Mechanism. *Top. Catal.* **2011**, *54*, 845.

(9) Grabow, L. C.; Gokhale, A. A.; Evans, S. T.; Dumesic, J. A.; Mavrikakis, M. Mechanism of the Water Gas Shift Reaction on Pt: First Principles, Experiments, and Microkinetic Modeling. *J. Phys. Chem. C* **2008**, *112*, 4608.

(10) Gokhale, A. A.; Dumesic, J. A.; Mavrikakis, M. On the Mechanism of Low-Temperature Water Gas Shift Reaction on Copper. *J. Am. Chem. Soc.* **2008**, *130*, 1402.

(11) Tranca, D. C.; Hansen, N.; Swisher, J. A.; Smit, B.; Keil, F. J. Combined Density Functional Theory and Monte Carlo Analysis of Monomolecular Cracking of Light Alkanes Over H-ZSM-5. *J. Phys. Chem. C* **2012**, *116*, 23408.

(12) Dumesic, J. A.; Huber, G. W.; Boudart, M. Microkinetics: Rates of Catalytic Reactions. In *Handbook of Heterogeneous Catalysis*; Ertl, G., Knozinger, H., Schuth, F., Weitkamp, J., Eds.; Wiley-VCH: New York, 2008; Vol. 3, Part 5, Section 5.2.1.

(13) Dumesic, J. A.; Rudd, D. F.; Aparicio, L. M.; Rekoske, J. E.; Trevino, A. A. *The Microkinetics of Heterogeneous Catalysis*; American Chemical Society: Washington, DC, 1993.

(14) Maestri, M.; Reuter, K. Molecular-level understanding of WGS and reverse WGS reactions on Rh through hierarchical multiscale approach. *Chem. Eng. Sci.* **2012**, *74*, 296.

(15) Maestri, M.; Vlachos, D. G.; Beretta, A.; Groppi, G.; Tronconi, E. Steam and Dry Reforming of Methane on Rh: Microkinetic Analysis and Hierarchy of Kinetic Models. *J. Catal.* **2008**, *259*, 211.

(16) Salciccioli, M.; Stamatakis, M.; Caratzoulas, S.; Vlachos, D. G. A review of multiscale modeling of metal-catalyzed reactions: Mechanism development for complexity and emergent behavior. *Chem. Eng. Sci.* **2011**, *66*, 4319.

(17) Chin, Y. H.; Buda, C.; Neurock, M.; Iglesia, E. Selectivity of chemisorbed oxygen in C−H bond activation and CO oxidation and kinetic consequences for CH_4−O_2 catalysis on Pt and Rh clusters. *J. Catal.* **2011**, *283*, 10.

(18) Van Santen, R. A.; Neurock, M. Concepts in Theoretical Heterogeneous Catalytic Reactivity. *Catal. Rev.: Sci. Eng.* **1995**, *37*, 557.

(19) Sabbe, M. K.; Reyniers, M. F.; Reuter, K. First-principles kinetic modeling in heterogeneous catalysis: An industrial perspective on best-practice, gaps and needs. *Catal. Sci. Technol.* **2012**, *2*, 2010.

(20) Feibelman, P. J. DFT Versus the "Real World" (or, Waiting for Godft). *Top. Catal.* **2010**, *53*, 417.

(21) Mei, D. H.; Hansen, E. W.; Neurock, M. Ethylene Hydrogenation over Bimetallic Pd/Au(111) Surfaces: Application of Quantum Chemical Results and Dynamic Monte Carlo Simulation. F. *Phys. Chem. B* **2003**, *107*, 798.

(22) Raimondeau, S.; Vlachos, D. G. Recent developments on multiscale, hierarchical modeling of chemical reactors. *Chem. Eng. J.* **2002**, *90*, 3.

(23) Vlachos, D. G.; Mhadeshwar, A. B.; Kaisare, N. S. Hierarchical multiscale model-based design of experiments, catalysts, and reactors for fuel processing. *Comput. Chem. Eng.* **2006**, *30*, 1712.

(24) Hansen, E. W.; Neurock, M. First-principles-based Monte Carlo simulation of ethylene hydrogenation kinetics on Pd. *J. Catal.* **2000**, *196*, 241.

(25) Neurock, M.; Hansen, E. W. First-principles-based molecular simulation of heterogeneous catalytic surface chemistry. *Comput. Chem. Eng.* **1998**, *22*, S1045.

(26) Donazzi, A.; Maestri, M.; Micheal, B.; Beretta, A.; Forzatti, P.; Groppi, G.; Tronconi, E.; Schmidt, L. D.; Vlachos, D. G. Microkinetic modeling of spatially resolved autothermal CH_4 catalytic partial oxidation experiments over Rh-coated foams. *J. Catal.* **2010**, *275*, 270.

(27) Maestri, M. Microkinetic Analysis of Complex Chemical Processes at Surfaces. In *New Strategies in Chemical Synthesis and Catalysis*; Pignataro, B., Ed.; Wiley-VCH: Weinheim, Germany, 2012; pp 219−246.

(28) Dumesic, J. A. Analyses of Reaction Schemes Using De Donder Relations. *J. Catal.* **1999**, *185*, 496.

(29) Dumesic, J. A. Reply to Finding the Rate-Determining Step in a Mechanism: Comparing DeDonder Relations with the "Degree of Rate Control". *J. Catal.* **2001**, *204*, 525.

(30) Campbell, C. T. Finding the Rate-Determining Step in a Mechanism: Comparing DeDonder Relations with the "Degree of Rate Control". *J. Catal.* **2001**, *204*, 520.

(31) Donazzi, A.; Beretta, A.; Groppi, G.; Forzatti, P. Catalytic partial oxidation of methane over a 4% $Rh/\alpha\text{-}Al_2O_3$ catalyst: Part I: Kinetic study in annular reactor. *J. Catal.* **2008**, *255*, 241.

(32) Donazzi, A.; Beretta, A.; Groppi, G.; Forzatti, P. Catalytic partial oxidation of methane over a 4% $Rh/\alpha\text{-}Al_2O_3$ catalyst Part II: Role of CO_2 reforming. *J. Catal.* **2008**, *255*, 259.

(33) Beretta, A.; Baiardi, P.; Prina, D.; Forzatti, P. Analysis of a catalytic annular reactor for very short contact times. *Chem. Eng. Sci.* **1999**, *54*, 765.

(34) Maestri, M.; Cuoci, A. CatalyticFOAM, www.catalyticfoam.polimi.it (accessed June 2014).

(35) Maestri, M.; Cuoci, A. Coupling CFD with detailed microkinetic modeling in heterogeneous catalysis. *Chem. Eng. Sci.* **2013**, *96*, 106.

(36) Beretta, A.; Donazzi, A.; Groppi, G.; Forzatti, P.; Dal Santo, V.; Sordelli, L.; De Grandi, V.; Psaro, R. Testing in annular micro-reactor and characterization of supported Rh nanoparticles for the catalytic partial oxidation of methane: Effect of the preparation procedure. *Appl. Catal. B* **2008**, *83*, 96.

(37) Maestri, M.; Reuter, K. Semi-empirical Rate Constants for Complex Chemical Kinetics: First-Principles Assessment and Rational Refinement. *Angew. Chem., Int. Ed.* **2011**, *50*, 1194.

(38) Mhadeshwar, A. B.; Vlachos, D. G. Hierarchical, multiscale surface reaction mechanism development: CO and H_2 oxidation, water–gas shift, and preferential oxidation of CO on Rh. *J. Catal.* **2005**, *234*, 48.

(39) Michael, B. C.; Donazzi, A.; Schmidt, L. D. Effects of H_2O and CO_2 addition in catalytic partial oxidation of methane on Rh. *J. Catal.* **2009**, *265*, 117.

(40) Fourie, J. G.; Du Plessis, J. P. Effective and coupled thermal conductivities of isotropic open-cellular foams. *AIChE J.* **2004**, *50*, 547.

(41) Maestri, M.; Beretta, A.; Groppi, G.; Tronconi, E.; Forzatti, P. Comparison among structured and packed-bed reactors for the catalytic partial oxidation of CH_4 at short contact times. *Catal. Today* **2005**, *105*, 709.

(42) Horn, R.; Williams, K. A.; Degenstein, N. J.; Schmidt, L. D. Syngas by catalytic partial oxidation of methane on rhodium: Mechanistic conclusions from spatially resolved measurements and numerical simulations. *J. Catal.* **2006**, *242*, 92.

(43) Donazzi, A.; Michael, B. C.; Schmidt, L. D. Chemical and geometric effects of Ce and washcoat addition on catalytic partial oxidation of CH_4 on Rh probed by spatially resolved measurements. *J. Catal.* **2008**, *260*, 270.

(44) Korup, O.; Goldsmith, C. F.; Weinberg, G.; Geske, M.; Kandemir, T.; Schlogl, R.; Horn, R. Catalytic partial oxidation of methane on platinum investigated by spatial reactor profiles, spatially resolved spectroscopy, and microkinetic modeling. *J. Catal.* **2013**, *297*, 1.

(45) Maestri, M.; Vlachos, D. G.; Beretta, A.; Forzatti, P.; Groppi, G.; Tronconi, E. Dominant reaction pathways in the catalytic partial oxidation of methane on Rh. *Top. Catal.* **2009**, *52*, 1983.

(46) Wei, J. M.; Iglesia, E. Structural requirements and reaction pathways in methane activation and chemical conversion catalyzed by rhodium. *J. Catal.* **2004**, *225*, 116.

(47) Wei, J. M.; Iglesia, E. Isotopic and kinetic assessment of the mechanism of reactions of CH_4 with CO_2 or H_2O to form synthesis gas and carbon on nickel catalysts. *J. Catal.* **2004**, *224*, 370.

(48) Shustorovich, E.; Sellers, H. The UBI-QEP method: A practical theoretical approach to understanding chemistry on transition metal surfaces. *Surf. Sci. Rep.* **1998**, *31*, 5.